Chiral Electron-Hole Pairing as the Origin of Anomalous Quasiparticle Dispersions in Unconventional Superconductors

Wanpeng Tan *

Posted Date: 28 February 2026

doi: 10.20944/preprints202602.2052.v1

Keywords: BCS; superconductivity; chiral condensation; dispersion; Bogoliubov quasiparticles; pairing mechanism

 doi:10.20944/preprints202602.2052.v1

Article

Chiral Electron-Hole Pairing as the Origin of Anomalous Quasiparticle Dispersions in Unconventional Superconductors

Wanpeng Tan

Department of Physics and Astronomy, University of Notre Dame, Notre Dame, Indiana 46556, USA; wtan@nd.edu

Abstract

The microscopic pairing mechanism in unconventional superconductors remains elusive, largely because the extreme flatness of the superconducting band often obscures key energy-momentum dispersion features observed in angle-resolved photoemission spectroscopy. In this work, we re-examine high-resolution dispersion data from cuprates (Bi2212 and Bi2201) and iron-based superconductors (monolayer FeSe) to test the predictions of a newly proposed chiral electron-hole (CEH) pairing mechanism. Unlike Cooper pairs in BCS-like theories that form a single quasiparticle band with a smooth back-bending dispersion, CEH pairs exhibit a distinct two-band structure in quasiparticle dispersion with sharp cusps at the back-bending points. Our analysis identifies clear empirical signatures of these CEH-predicted features, concluding that quasiparticle dispersions in these strongly correlated materials deviate significantly from BCS-like behavior. Further comprehensive and targeted experimental strategies are proposed to definitively resolve the subtle dispersion features and rigorously test the CEH model for unconventional superconductivity.

Keywords: BCS; superconductivity; chiral condensation; dispersion; Bogoliubov quasiparticles; pairing mechanism

1. Introduction

Angle-resolved photoemission spectroscopy (ARPES) [1] has emerged as an indispensable technique in the study of unconventional superconductors. Notably, it has been instrumental in determining superconducting gap symmetries, such as the discovery of the $d_{x^2-y^2}$ d-wave gap symmetry in cuprates [2]. Moreover, ARPES serves as a powerful tool for elucidating the band structures of superconducting materials, particularly by revealing the energy-momentum dispersion of the quasiparticles responsible for superconductivity.

The two primary classes of high-T_c superconductors — cuprate [3] and iron-based (FeSC) [4] materials — exhibit behaviors that diverge fundamentally from those of conventional superconductors that are well described by Bardeen-Cooper-Schrieffer (BCS) theory [5]. Both cuprates and FeSCs are strongly correlated electronic systems proximate to their antiferromagnetic (AFM) parent compounds, and many of their properties evade explanation within traditional BCS or BCS-like frameworks. Despite this, a 2003 ARPES study reported evidence of BCS-like quasiparticle dispersion in nearly optimally doped Bi-2223 ($T_c = 108$ K) [6]. A crucial caveat to this claim, however, is that at temperatures $T \ll T_c$, the associated band for such nearly perfect superconductors is exceedingly flat relative to the instrumental resolution of ARPES, rendering it incapable of definitively distinguishing between different types of dispersion relations.

In this work, we utilize more recently published high-resolution ARPES data [7–11] to demonstrate that the quasiparticle dispersions in cuprates and FeSCs deviate significantly from BCS-like behavior. Instead, the observed dispersion features align closely with the predictions of a recently proposed pairing mechanism driven by chiral electron-hole (CEH) condensation [12]. The CEH framework intrinsically necessitates strongly correlated AFM materials for non-BCS superconductivity.

 doi:10.20944/preprints202602.2052.v1

Furthermore, it accounts for numerous puzzling properties observed in cuprates and FeSCs, including the pseudogap phenomenon, the absence of gap closure at T_c, unexpectedly large Δ_0/T_c ratios, and a non-zero $\gamma(0)$ term and a quadratic temperature dependence in the specific heat ratio C/T as $T \to 0$ in d-wave cuprates [12].

In the subsequent sections, we first outline the CEH pairing mechanism and analyze its unique predicted dispersion features, specifically the emergence of two-band structures and cusps at the back-bending points. We then present and discuss detailed comparisons with recent high-resolution ARPES measurements. Ultimately, these comparisons provide compelling evidence for further systematic investigations to verify the theoretical predictions of the CEH model.

2. Chiral Electron-Hole (CEH) Pairing

To introduce the CEH pairing mechanism within a mean-field framework, we begin with a four-fermion interacting Hamiltonian,

$$H = \sum_{\mathbf{k}\sigma} \xi_{\mathbf{k}} c^{\dagger}_{\mathbf{k}\sigma} c_{\mathbf{k}\sigma} - V \sum_{\mathbf{k}\mathbf{k}'} c^{\dagger}_{\mathbf{k}L} c_{-\mathbf{k}R} c^{\dagger}_{-\mathbf{k}'R} c_{\mathbf{k}'L} \tag{1}$$

where $\xi_{\mathbf{k}}$ denotes the single-particle energy relative to the Fermi surface, assuming perfect particle-hole and chiral symmetries. Note that left (L) and right (R) chiralities are used here to replace the conventional up and down spin notation.

Traditional BCS theory postulates that a system becomes superconducting due to the condensation of electron-electron Cooper pairs $\langle c_{\mathbf{k}L} c_{-\mathbf{k}R} \rangle$. In the new CEH model, however, superconductivity arises from the condensation of chiral electron-hole pairs, with the corresponding order parameter $\mathbf{\Delta}$ defined as,

$$\mathbf{\Delta} = V \sum_{\mathbf{k}} \langle c^{\dagger}_{\mathbf{k}L} c_{-\mathbf{k}R} \rangle \,, \quad \mathbf{\Delta}^* = V \sum_{\mathbf{k}} \langle c^{\dagger}_{-\mathbf{k}R} c_{\mathbf{k}L} \rangle \,. \tag{2}$$

This leads to the following Bogoliubov-de Gennes (BdG) Hamiltonian,

$$H = \sum_{\mathbf{k}} \begin{pmatrix} c^{\dagger}_{\mathbf{k}L}, & c^{\dagger}_{-\mathbf{k}R} \end{pmatrix} \begin{pmatrix} \xi_{\mathbf{k}} & -\mathbf{\Delta}^* \\ -\mathbf{\Delta} & \xi_{\mathbf{k}} \end{pmatrix} \begin{pmatrix} c_{\mathbf{k}L} \\ c_{-\mathbf{k}R} \end{pmatrix} + \frac{|\mathbf{\Delta}|^2}{V}. \tag{3}$$

which can be diagonalized via the Bogoliubov transformation. The resulting eigen-energies of the Bogoliubov CEH quasiparticles are

$$E^{\pm}_{\mathbf{k}} = \xi_{\mathbf{k}} \pm |\mathbf{\Delta}|, \tag{4}$$

which contrasts sharply with the standard BCS-like dispersion relation, $E^{\pm}_{\mathbf{k}} = \pm\sqrt{\xi^2_{\mathbf{k}} + |\mathbf{\Delta}|^2}$. This striking difference in energy-momentum dispersion constitutes the primary focus of this paper.

It is worth noting that both the BCS and CEH mechanisms for superconductivity bear conceptual similarities to neutrino or neutron–mirror neutron oscillations [13,14], originating from the unitary mixing between misaligned interaction and energy eigenstates. A particularly intriguing reciprocal relationship exists between the two models: the energy eigenstates of Cooper pairs are a superposition of two CEH-pair-like particles (i.e., mixing of chirally opposite electrons and holes), whereas the energy eigenstates of CEH pairs are a superposition or mixing of two Cooper-pair-like electrons or holes.

A fundamental distinction between the two models is that BCS quasiparticles are characterized by a single energy branch, $\sqrt{\xi^2_{\mathbf{k}} + |\mathbf{\Delta}|^2}$, whereas CEH quasiparticles possess two distinct energy branches, $|\mathbf{\Delta}| \pm |\xi_{\mathbf{k}}|$, resulting in a two-band structure and cusps at the back-bending points. In addition, the Bogoliubov mixing angle in BCS theory, defined as $\theta^{\mathrm{BCS}}_{\mathbf{k}} = \arctan|v_{\mathbf{k}}/u_{\mathbf{k}}|$, varies greatly between 0 and $\pi/2$ satisfying $\tan(2\theta_{\mathbf{k}}) = -|\mathbf{\Delta}|/\xi_{\mathbf{k}}$. In contrast, the CEH mixing angle, $\theta^{\mathrm{CEH}}_{\mathbf{k}}$, remains constant at $\pi/4$ as $|u| = |v| = 1/\sqrt{2}$ assuming perfect chiral symmetry with $\xi_{\mathbf{k}L} = \xi_{\mathbf{k}R}$.

Depending on the orbital pairing symmetry, the CEH mechanism can yield an angular-dependent superconducting energy gap, $\Delta_{\mathbf{k}} \equiv |\mathbf{\Delta}_{\mathbf{k}}| = \Delta\gamma_{\mathbf{k}}$. For the $d_{x^2-y^2}$ d-wave gap symmetry typical of

 doi:10.20944/preprints202602.2052.v1

cuprate superconductors, the symmetry factor $\gamma_{\mathbf{k}} = |\cos k_x a - \cos k_y b|/2$ can be approximated as $\cos(2\varphi)$. This substitution leads to the following d-wave CEH gap equation [12],

$$\Delta(T) = \frac{8\lambda T}{\pi}\int_0^{\pi/4} d\varphi \, \tanh^{-1}\left(\tanh(\frac{\Delta(T)\cos(2\varphi)}{2T})\tanh(\frac{\omega^*}{2T})\right) \tag{5}$$

where the single-particle energy is integrated over the flat band (defined by $\pm\omega^*$ around the fermi surface), and $\lambda = V\rho_F$ represents the dimensionless coupling constant. Strikingly, this d-wave gap equation requires $\lambda > \pi/2$ (or $\lambda > 1$ for s-wave), indicating that the CEH mechanism is intrinsically suited for strongly correlated electron systems [12].

In the presence of chiral asymmetry, the modified dispersion and the Bogoliubov mixing angle can be expressed as,

$$E_{\mathbf{k}}^{\pm} = \frac{\zeta_{\mathbf{k}L}+\zeta_{\mathbf{k}R}}{2} \pm \sqrt{\Delta_{\mathbf{k}}^2 + \left(\frac{\zeta_{\mathbf{k}L}-\zeta_{\mathbf{k}R}}{2}\right)^2}, \tag{6}$$

$$\tan\theta_{\mathbf{k}}^{\mathrm{CEH}} = \sqrt{1+\left(\frac{\zeta_{\mathbf{k}L}-\zeta_{\mathbf{k}R}}{\Delta_{\mathbf{k}}}\right)^2} - \frac{\zeta_{\mathbf{k}L}-\zeta_{\mathbf{k}R}}{\Delta_{\mathbf{k}}}. \tag{7}$$

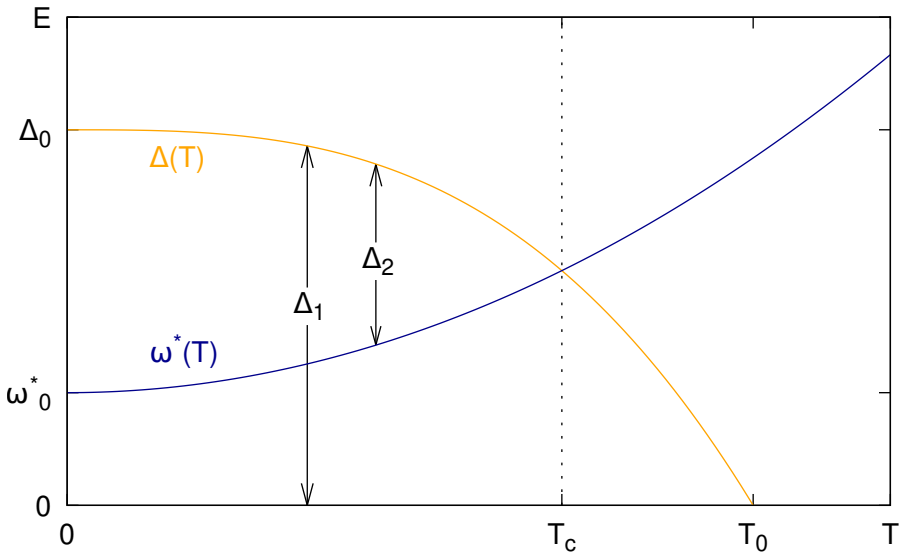

Figure 1. Schematic diagram illustrating the temperature dependence of the superconducting gap Δ and the flat-band width ω^* with the two-gap structure of $\Delta_1 = \Delta$ and $\Delta_2 = \Delta - \omega^*$. The critical temperature, T_c, is defined as the point where the band width equals the superconducting gap or $\Delta_2 = 0$, while T_0 denotes the gap-closing temperature ($\Delta_1 = 0$).

It is important to emphasize that the CEH pairing mechanism favors antiferromagnetism, and strong electronic correlations inherently lead to its non-local behavior. While it is well established that the superconducting gap decreases as temperature increases, the flat-band width, ω^*, may also exhibit temperature dependence, becoming flatter at lower temperatures as illustrated in the schematic diagram of Figure 1. Crucially, the onset of superconductivity requires [12],

$$\omega^*(T) \leq \Delta(T), \tag{8}$$

meaning that the band ($\pm\omega^*$) in which the CEH quasiparticles form must be sufficiently flat so as not to exceed the superconducting gap Δ. No analogous requirement exists within BCS theory. Consequently, in the CEH framework, the critical temperature T_c is defined by the condition $\omega^*(T_c) = \Delta(T_c)$, whereas the gap-closing temperature T_0 is defined by $\Delta(T_0) = 0$.

 doi:10.20944/preprints202602.2052.v1

3. energy-momentum dispersion

An optimal strategy for distinguishing the CEH quasiparticle dispersion from other BCS-like models involves conducting high-resolution ARPES measurements along the Brillouin zone (BZ) boundary, traversing an antinode and two adjacent Fermi surfaces in cuprates. In this momentum region, the unique spectral features predicted by the CEH model become pronounced. Specifically, because the two Fermi surfaces are in close proximity, the d-wave superconducting gap is near its maximum and approximately constant, allowing the single-particle dispersion to be well modeled by a parabola. Consequently, the observation of cusps at the back-bending points, alongside a distinct two-band structure, would provide definitive evidence for the CEH mechanism.

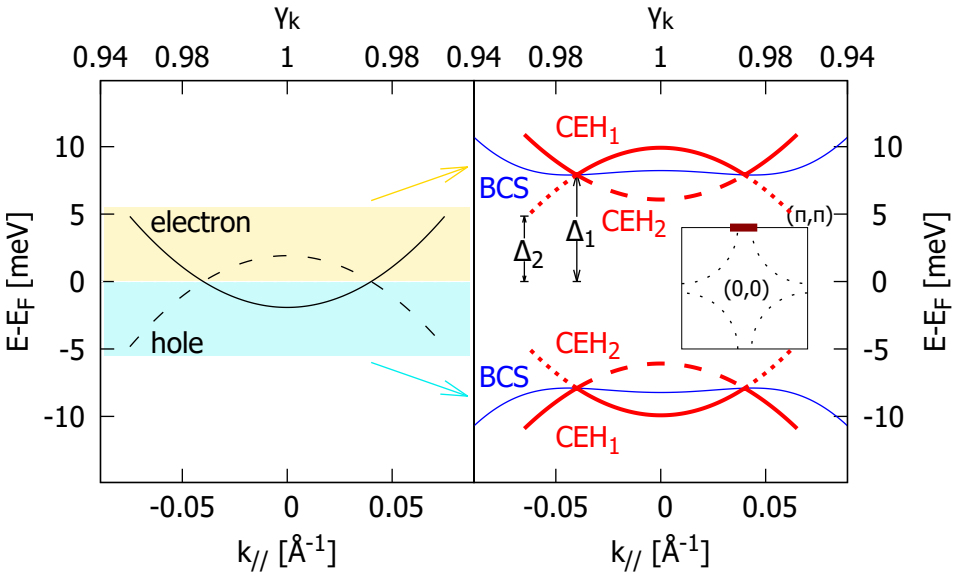

Figure 2. Schematic comparison of the energy-momentum dispersions transitioning from the normal state (left panel) to the gapped superconducting phase (right panel) for both the CEH and BCS-like models. $\gamma_{\mathbf{k}}$ is calculated for Bi-2212. The thick red bar traversing the $(0,\pi)$ antinode in the BZ inset indicates the momentum cut corresponding to the displayed dispersions.

A schematic representation of the first Brillouin zone for the 2D CuO_2 layer is provided in the right-panel inset of Figure 2. The thick red bar along the BZ boundary, which crosses the $(0,\pi)$ antinode, indicates the momentum trajectory along which the energy-momentum dispersion is analyzed here. This cut lies also within the AFM zone and yields a nearly constant d-wave superconducting gap, characterized by the symmetry factor $\gamma_{\mathbf{k}} = (\cos k_{\|} a + 1)/2 \simeq 1$ (e.g., lattice constants $a = b = 5.4$Å for Bi-2212 superconductors).

Figure 2 illustrates the normal-state and quasiparticle energy bands relative to the Fermi level as a function of the parallel momentum along the cut and the corresponding d-wave symmetry factor $\gamma_{\mathbf{k}}$. On the left panel, the solid and dashed parabolas represent the normal-state dispersion for the electron and hole branches, respectively, residing within a relatively flat band and assuming perfect particle-hole symmetry. In the superconducting state, depicted on the right panel, a gap opens, yielding a single quasiparticle band in each branch according to a BCS-like theory (indicated by the blue lines).

In contrast, the CEH mechanism generates two distinct quasiparticle bands within each branch (denoted by solid red lines for band 1, and dashed/dotted red lines for band 2). In the superconducting phase, the primary CEH quasiparticle dispersion (band 1, representing the more energetic quasiparticles) is governed by,

$$E - E_F = \pm(|\Delta_{\mathbf{k}}| + |\xi_{\mathbf{k}}|) \tag{9}$$

which shows distinct, sharp cusps at the back-bending points, fundamentally differing from the smooth transitions characteristic of BCS-like dispersions. Most remarkably, unlike the BCS framework where

 doi:10.20944/preprints202602.2052.v1

quasiparticles share one single dispersion, CEH quasiparticles split into two distinct energy branches. The less energetic quasiparticles form a secondary band (band 2) governed by,

$$E - E_F = \pm(|\Delta_{\mathbf{k}}| - |\xi_{\mathbf{k}}|). \tag{10}$$

Consequently, as illustrated in Figure 2, two corresponding energy gaps (Δ_1 and Δ_2) are associated with these distinct quasiparticle bands.

This two-gap feature, inherent to the CEH model and possibly first observed in La-Bi2201 in 2008 [15], naturally accounts for the pseudogap phenomenon, particularly given that $\Delta_1 = \Delta$ does not vanish above T_c. As such, macroscopic superconductivity emerges only when $\Delta_2 = \Delta - \omega^* > 0$, a criterion identical to the condition established in Eq. 8. It also clarifies why relatively flat bands (characterized by smaller ω^*) are a necessary precondition for CEH-driven superconductivity.

While the primary band (band 1) has been observed in many prior studies, explicit evidence of cusps at the back-bending points has remained elusive. This is largely attributable to limitations in ARPES resolution relative to the extreme flatness of these bands. Empirical evidence for band 2 (the dashed and dotted red lines in Figure 2) is even more scarce within the existing literature. In the following analysis, we present renewed evidence for both features utilizing recently published, high-resolution ARPES data.

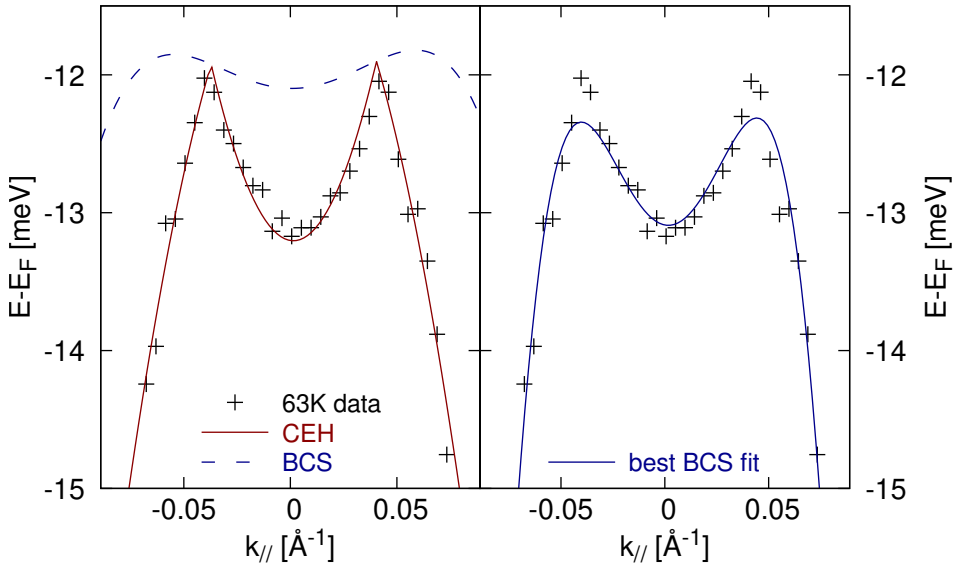

Figure 3. Quasiparticle dispersion at $T = 63$ K (just below $T_c = 66$ K) for the Bi-2212 sample OD66, utilizing data from Ref. [7]. Left: The CEH dispersion (solid red curve) yields an excellent fit to the experimental data; the corresponding BCS-like dispersion (dashed blue curve) is shown for comparison. Right: The best BCS-like fit (solid blue curve) fails to reproduce the observed cusps at the back-bending points.

 doi:10.20944/preprints202602.2052.v1

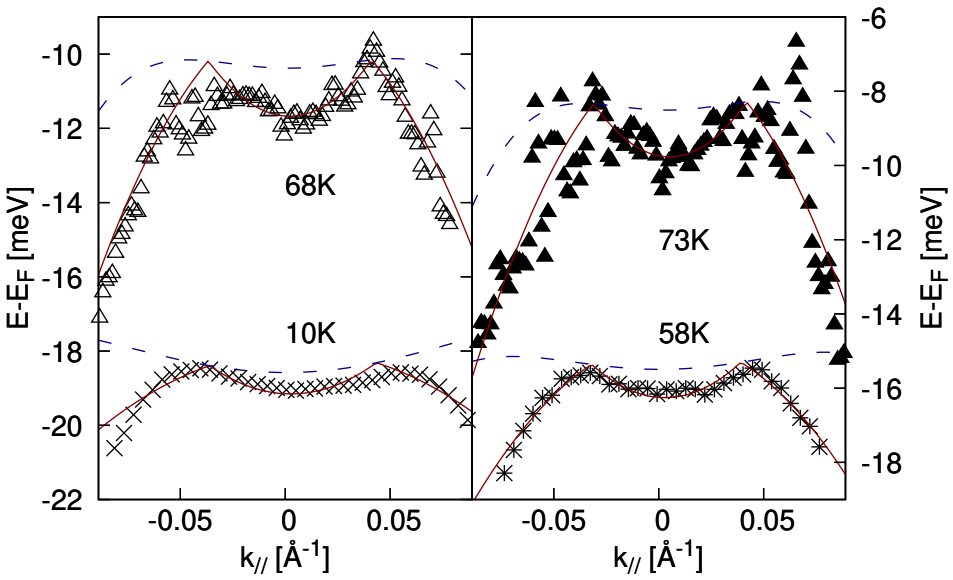

Figure 4. Quasiparticle dispersions at other temperatures for the Bi-2212 sample OD66, with data from Ref. [7]. The CEH dispersions (solid red curves) fit the data well, particularly in reproducing the back-bending cusps, with the notable exception of the 10 K measurement. BCS-like dispersions (dashed blue curves), calculated using the fitted normal-state dispersion, are provided for comparison.

Compelling evidence for the presence of cusps in band 1 is presented in Figure 3, which displays the dispersion measured near T_c for the Bi-2212 sample OD66 [7]. This data is fitted under the assumption of a simple parabolic normal-state dispersion, implying robust chiral and particle-hole symmetries. The CEH dispersion (solid red curve, left panel) demonstrates excellent agreement with the experimental data. Conversely, the best BCS-like fit (solid blue curve, right panel) fails to reproduce the cusps at the back-bending points and it artificially requires a significantly steeper normal-state dispersion, comparable to the measurements taken at $T = 145$ K, which is at odds with the evidence discussed below.

Dispersions and corresponding fits at various other temperatures for the same OD66 sample are detailed in Figure 4. Because the superconducting gap is nearly constant in this momentum region, the extended "wings" beyond the back-bending points predominantly dictate the shape of the underlying single-particle (hole) parabolic dispersion that should agree with its electron counterpart determined by the quasiparticle dispersion in between the back-bending points assuming particle-hole symmetry. Notably, the band flattens at lower temperatures, indicative of an increasing effective mass as the system cools.

The measurement at $T = 63$ K provides the clearest resolution of the cusp feature by striking an optimal balance between minimized experimental uncertainty and a band that is not yet excessively flat compared to lower-temperature data (as shown in Figure S1). Consequently, fits at other temperatures are comparatively less definitive. Specifically, the fit at $T = 10$ K is limited by the extreme flatness of the band at such a low temperature. The extracted normal-state dispersions at these temperatures with fitting parameters summarized in Table A1 are plotted in Figure S2, consistently demonstrating the progressive flattening of the band as temperature decreases. This temperature-dependent flattening is independently corroborated by the findings in Figs. 3i–j and S13a–b of Ref. [7], which show that the normal-state dispersion at 86 K (where the gap is nearly closed) is substantially flatter than the one at 145 K.

 doi:10.20944/preprints202602.2052.v1

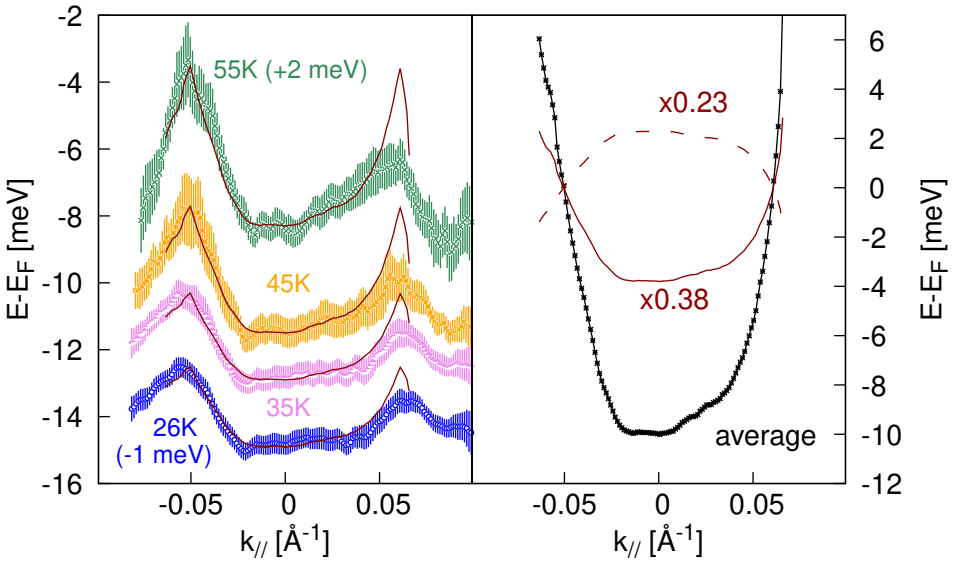

Figure 5. Left: Dispersion data at varied temperatures for the Bi-2212 sample OD49 from Ref. [7], overlaid with CEH fits (red curves). Select datasets are offset as labeled for clarity. Right: Average normal-state dispersion data (black stars) acquired between 65 K and 95 K (from Fig. S14b of Ref. [7]), and its scaling demonstration for a representative CEH fit at $T = 45$ K, which uses the solid and dashed red curves with band scaling factors of 0.38 and 0.23 for the electron and hole normal states, respectively.

Further evidence of cusps in band 1 is provided in Figure 5 with fitting parameters summarized in Table A2, displaying data for the Bi-2212 sample OD49 [7]. Here, the dispersions exhibit even more pronounced cusps due to the reduced flatness of the superconducting band. However, this sample also presents stronger chiral and particle-hole asymmetries. To better fit the quasiparticle dispersion, an averaged experimental normal-state dispersion (black stars in the right panel of Figure 5), measured at higher temperatures, is scaled down, using distinct scaling factors for the electron and hole branches to account for the band flatness at lower temperatures. Such scaling is demonstrated for the 45-K fit on the right panel. The discrepancies observed at the right back-bending points likely originate from misaligned single-particle dispersions or other distortions near the Fermi level (unaccounted in the fitting), which is also visible, albeit to a much lesser extent, in the OD66 data (Figure S1).

 doi:10.20944/preprints202602.2052.v1

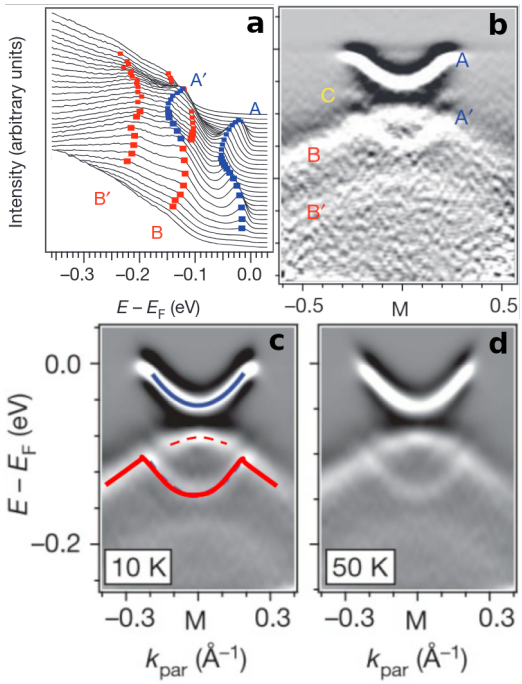

Figure 6. Quasiparticle band dispersions intersecting an electron pocket centered at the M-point for monolayer FeSe on $SrTiO_3$ [8]. (a) EDCs presented as a waterfall plot. (b) Second-derivative intensity plot at 16 K, with bands labeled corresponding to (a). (c,d) Intensity plots at different temperatures; the solid red curve traces CEH band 1, while the dashed red line indicates CEH band 2. Adapted from Figs. 1 and 3 of Ref. [8].

Arguably the most comprehensive evidence capturing the features of both CEH bands is found in the ARPES data (Figure 6) for superconducting monolayer FeSe films grown on $SrTiO_3$ [8]. These spectra were acquired along a momentum cut through an electron pocket centered at the M-point, which is analogous to the antinodal cut analyzed in the cuprates. CEH band 1 traced by the solid red curve and band 2 indicated by the dashed red line in Figure 6c, originally conflated as labels A′ and B in the source reference, are both clearly resolved. Because these bands are situated deeply ($\sim$ 100 meV below the Fermi surface) and lack the extreme flatness seen in cuprates, the signature CEH features are starkly visible. Although the band closer to the Fermi surface (band A, marked by the blue line) is the one primarily responsible for superconductivity in this system, the authors of Ref. [8] convincingly demonstrated that these deeper CEH bands are exclusively associated with superconducting monolayer FeSe and are entirely absent in non-superconducting multilayer samples.

These quasiparticle dispersion relations in FeSe are further illustrated by the waterfall plot of energy distribution curves (EDCs) in Figure 6a [8]. In this representation, the central segment of CEH band 2 (corresponding to the dashed red lines in Figures 2 and 6c) manifests clearly as a structural shoulder next to CEH band 1. Intriguingly, similar shoulder features have been reported in the literature for other superconductors. For instance, the data for Bi-2201 shown in Figure S3 [9] explicitly display this shoulder feature characteristic of band 2, and simultaneously exhibit indications of cusps in band 1. The shoulder feature becomes more pronounced at lower temperatures, as illustrated in similar plots in Figs. 2 and 4 of Ref. [9], Fig. 1 of Ref. [10], and Fig. 4 of Ref. [11].

Despite these observations, the extended "wings" of band 2 (represented by the dotted red lines in Figure 2) seem to be much less discernible in published data. A weak spectral feature (labeled as band C in Figure 6b) may offer tentative evidence of their existence. More inspiringly, the temperature-dependent ARPES spectra and EDC plots from Ref. [7] (Figs. 3e-h and S13c-f therein) reveal ridges crossing the Fermi surfaces that start to develop near or above T_c. These ridges could plausibly represent the emerging wings of band 2. Future investigations, particularly those leveraging advanced ARPES image-processing techniques, are essential to definitively isolate and clarify this subtle spectral feature.

 doi:10.20944/preprints202602.2052.v1

4. Conclusions and Outlook

We have re-examined previously published data to present compelling evidence for the unique two-band structure and cusp features in quasiparticle dispersion, as predicted by the recently proposed chiral electron-hole pairing mechanism for non-BCS superconductivity. To further validate these findings, future high-precision ARPES studies are essential, particularly those focused on the antinodal cut along the BZ boundary in cuprates and the M-point cut in FeSCs. Comprehensive and systematic measurements of these materials across a wider range of doping levels and temperatures are highly encouraged. Specifically, to make signatures like the back-bending cusps more pronounced, experimental efforts should target underdoped or sub-optimal superconductors near T_c, where the associated superconducting bands exhibit reduced flatness. Finally, to better visualize and extract these complex quasiparticle dispersions, analyses must move beyond the simple fitting of EDC maxima. The application of advanced techniques such as the second-derivative approach, the curvature method [16], and possibly machine learning algorithms and emerging AI technology, will be critical for definitively resolving these subtle spectral features in future research.

Supplementary Materials: The following supporting information can be downloaded at the website of this paper posted on Preprints.org.

Acknowledgments: This work is supported in part by the faculty research support program at the University of Notre Dame. We extend our gratitude to Sudi Chen for valuable early discussions, and to both Sudi Chen and Yu He for generously providing the tabulated data used in their publication [7].

Appendix A

Table A1. CEH fitting parameters for Figures 3-4.

T [K]	normal-state parabola [meV]	Δ [meV]
10	$371.27(k_{\|\|}+0.03609)(k_{\|\|}-0.04341)$	18.57
58	$618.15(k_{\|\|}+0.03198)(k_{\|\|}-0.03915)$	15.47
63	$771.14(k_{\|\|}+0.03720)(k_{\|\|}-0.04039)$	12.04
68	$916.06(k_{\|\|}+0.03667)(k_{\|\|}-0.04116)$	10.29
73	$1029.61(k_{\|\|}+0.03108)(k_{\|\|}-0.04188)$	8.40

Table A2. CEH fitting parameters for Figure 5.

T [K]	scaling factor for electron branch	scaling factor for hole branch	Δ [meV]
26	0.24	0.10	11.5
35	0.26	0.12	10.3
45	0.38	0.23	7.7
55	0.48	0.36	5.5

References

1. J. A. Sobota, Y. He, and Z.-X. Shen, Rev. Mod. Phys. **93**, 025006 (2021).
2. Z.-X. Shen, D. S. Dessau, B. O. Wells, D. M. King, W. E. Spicer, A. J. Arko, D. Marshall, L. W. Lombardo, A. Kapitulnik, P. Dickinson, S. Doniach, J. DiCarlo, T. Loeser, and C. H. Park, Phys. Rev. Lett. **70**, 1553 (1993).
3. J. G. Bednorz and K. A. Müller, Z. Physik B - Condensed Matter **64**, 189 (1986).
4. Y. Kamihara, H. Hiramatsu, M. Hirano, R. Kawamura, H. Yanagi, T. Kamiya, and H. Hosono, J. Am. Chem. Soc. **128**, 10012 (2006).
5. J. Bardeen, L. N. Cooper, and J. R. Schrieffer, Phys. Rev. **106**, 162 (1957).
6. H. Matsui, T. Sato, T. Takahashi, S.-C. Wang, H.-B. Yang, H. Ding, T. Fujii, T. Watanabe, and A. Matsuda, Phys. Rev. Lett. **90**, 217002 (2003).
7. Y. He, S.-D. Chen, Z.-X. Li, D. Zhao, D. Song, Y. Yoshida, H. Eisaki, T. Wu, X.-H. Chen, D.-H. Lu, and others, Phys. Rev. X **11**, 031068 (2021).
8. J. J. Lee, F. T. Schmitt, R. G. Moore, S. Johnston, Y.-T. Cui, W. Li, M. Yi, Z. K. Liu, M. Hashimoto, Y. Zhang, D. H. Lu, T. P. Devereaux, D.-H. Lee, and Z.-X. Shen, Nature **515**, 245 (2014).

 doi:10.20944/preprints202602.2052.v1

9. R.-H. He, M. Hashimoto, H. Karapetyan, J. D. Koralek, J. P. Hinton, J. P. Testaud, V. Nathan, Y. Yoshida, H. Yao, K. Tanaka, and others, Science **331**, 1579 (2011).
10. M. Hashimoto, R.-H. He, K. Tanaka, J.-P. Testaud, W. Meevasana, R. G. Moore, D. Lu, H. Yao, Y. Yoshida, H. Eisaki, T. P. Devereaux, Z. Hussain, and Z.-X. Shen, Nature Phys **6**, 414 (2010).
11. M. Hashimoto, I. M. Vishik, R.-H. He, T. P. Devereaux, and Z.-X. Shen, Nature Phys. **10**, 483 (2014).
12. W. Tan, Journal of Physics and Chemistry of Solids **193**, 112148 (2024).
13. W. Tan, Phys. Lett. B **797**, 134921 (2019), arXiv:1902.01837 .
14. W. Tan, Universe **9**, 180 (2023).
15. J.-H. Ma, Z.-H. Pan, F. C. Niestemski, M. Neupane, Y.-M. Xu, P. Richard, K. Nakayama, T. Sato, T. Takahashi, H.-Q. Luo, L. Fang, H.-H. Wen, Z. Wang, H. Ding, and V. Madhavan, Phys. Rev. Lett. **101**, 207002 (2008).
16. P. Zhang, P. Richard, T. Qian, Y.-M. Xu, X. Dai, and H. Ding, Rev. Sci. Instrum. **82**, 043712 (2011)